ACSNANO

www.acsnano.org

ARTICLE

Germanium Metasurfaces with Lattice Kerker Effect in Near-Infrared Photodetectors

Zhong-Xing Zhou,[#] Ming-Jyun Ye,[#] Min-Wen Yu, Jhen-Hong Yang, Kuan-Lin Su, Chung-Ching Yang, Cheng-Yeh Lin, Viktoriia E. Babicheva, Ivan V. Timofeev, and Kuo-Ping Chen*

Cite This: *ACS Nano* 2022, 16, 5994–6001

Read Online

ACCESS | Metrics & More | Article Recommendations | Supporting Information

ABSTRACT: **In O-and C-band optical communications, Ge is a promising material for detecting optical signals that are encoded into electrical signals. Herein, we study 2D periodic Ge metasurfaces that support optically induced electric dipole and magnetic dipole lattice resonances. By overlapping Mie resonances and electric dipole lattice resonances, we realize the resonant lattice Kerker effect and achieve narrowband absorption. This effect was applied to the photodetector demonstrated in this study. The absorptance of the Ge nanoantenna arrays increased 6-fold compared to that of the unpatterned Ge films. In addition, the photocurrent in such Ge metasurface photodetectors increases by approximately 5 times compared with that in plane Ge film photodetectors by the interaction of these strong near-fields with semiconductors and the further transformation of the optical energy into electricity.**

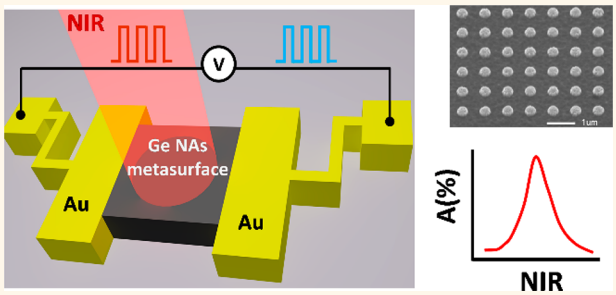

KEYWORDS: *germanium (Ge), high refractive index (HRI), dielectric nanoantennas, photodetector, metasurfaces, absorber*

Si-based technology has been widely studied, and photodetection involving Si designs has become a popular direction among researchers.[1−9] However, because of the transparency at the telecommunication wavelengths, which results in low absorption in the material, Si is unsuitable for detection at 1550 nm. Therefore, Ge is an ideal candidate for on-chip photodetection owing to its small bandgap of approximately 0.66 eV and compatibility with modern CMOS (complementary metal oxide semiconductor) technology. Ge has been widely used for near-infrared (NIR) photodetection.[10−18] However, the imaginary part of the refractive index of Ge significantly decreases from visible to NIR, which means that the quantum efficiency decreases as the wavelength increases.[19] To solve this problem, some researchers have pursued the engineering of high-quality Ge films using single-crystalline Ge nanomembranes (Ge NMs).[20,21] It uses epitaxy growth technology, and the material is produced by releasing Ge from an insulator wafer (GeOI).[22−24] For a Ge thin film, not only a low quantum efficiency but also a high surface recombination rate hinders the development of a compact and efficient photodetector. Research on the conventional p-i-n Ge detector has dominated in recent years.[25,26] During diffusion, the "dead layers" at the outer side of the detector are inactive regions, and the surface layer has a higher doping than the interior. This causes many crystallographic defects that act as recombination regions, and they reduce the detection efficiency.[27]

Therefore, it is important to overcome these challenges and achieve a high quantum efficiency at wavelengths near the absorptance edge. With optical near-field enhancement in particles, the quantum efficiency of the photodetector can be improved. Because of the high refractive index (HRI) of Ge, Ge nanoparticles can induce enhanced electric and magnetic resonances with a strong electromagnetic field in the particles as well as support Mie resonances in the NIR spectral range with the characteristic dimensions of 250−350 nm.[28−30] There are large forward and backward scattering signals of Mie resonances, and controlling the directional scattering of nanoparticles has been actively investigated in the recent years.[30−35] Using Mie theory for a spherical dielectric nanoparticle, the destructive interference between the electric dipole (ED) and magnetic dipole (MD) resonances results in scattering cancellation in the backward direction when the resonance wavelengths of the ED and MD are close to each other. This condition for zero backward scattering was derived in earlier works (by Kerker et al.[36]).

Received: December 20, 2021
Accepted: February 17, 2022
Published: February 22, 2022

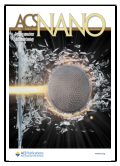

https://doi.org/10.1021/acsnano.1c11326
ACS Nano 2022, 16, 5994−6001

In this study, a Ge nanoantenna array (GNA) metasurface with high-efficiency absorption resonance at the telecommunication wavelength was proposed. An absorptance of ~70% at a wavelength of ~1550 nm was achieved in the GNA with a thickness of 300 nm, which is only 1/5 of the wavelength. By adjusting the lattice period of the GNA, the electric dipole lattice resonance (EDLR) can be controlled to overlap the MD resonances of antennas, called the lattice Kerker effect, in the NIR spectrum. The absorption of the GNA photodetector was effectively enhanced by overlapping resonance phenomena. Compared to the same thickness of a Ge film photodetector, the Ge metasurface demonstrated a 6-fold absorption enhancement in the NIR spectrum, corresponding to the numerical analysis and experimental results. Furthermore, we demonstrate nondoping (intrinsic) Ge metasurfaces for C-band photodetection and integration with Si photonic measurement systems. The photoresponsivity of the intrinsic Ge metasurfaces without the p-i-n structure can be 5 times better than that of thin-film devices. The GNA metasurfaces have proven to be promising selective photodetectors, and they encode electrical signals in the NIR spectrum. The Ge metasurface photodetector design has considerable applications in optical filters, sensing, NIR imaging, and telecommunications.

First, we consider a 2D array of particles arranged in periodic lattices. Owing to the coupling interaction between the nanoparticles, lattice resonance (LR) is excited and produces additional narrow resonant features when the period of the array is comparable to the wavelength of nanoparticle resonance.[37−40] For instance, when an electric field of the incident wave is along the x-axis, we can change the position and strength of EDLR by varying transverse array periods (in the y-direction). Similarly, the magnetic dipole lattice resonance (MDLR) excited in the y-direction can be controlled by the period in the x-direction. To tune the array period, the coupling between LR and the Mie resonance has been actively investigated in recent years.[41,42] The photodetector experimental results, including photocurrent and responsivity measurements in Figures 5 and 6, were consistent with the optical result at approximately 1550 nm shown in Figure S4. In ref. 22, Sebastian et al. theoretically showed a core−shell nanoparticle (silver shells with silica cores) with a radius below 100 nm and a high-quality factor above 500 in the visible range with plasmon hybridization. In ref. 23, a resonant lattice core−shell (silver in dielectric shell) model was simulated, whose Q-factor was over 500 in the visible spectrum. However, so far, it has been difficult to achieve such high quality with 2D periodic arrays and the Kerker effect in the NIR spectrum. In addition, there are the limitations of the fabrication, such as the structure roughness for etching and for the near-field effect in the nanostructure for E-beam lithography.

The quality factor of the resonance spectra in photocurrent responsivity was ~53 at the communication wavelength, and it was consistent with the absorptance of the photodetector in the simulation. Moreover, the redshift signal was caused by a slight tilt divergence angle in the optical and photocurrent measurement setup, as shown in the Supporting Information.

In this study, coupled dipole equations (CDEs) based on a periodic Green's function are used to theoretically study the resonances of spherical nanoparticles arranged in a periodic 2D array.[43−45] The particles in the equation are considered electric and magnetic dipoles with electric and magnetic polarizabilities α^E and α^M, respectively. α^E and α^M are defined as

$$\alpha^E = \frac{6\pi\varepsilon_0\varepsilon_d}{k_d^3} i a_1,\ \alpha^M = \frac{6\pi}{k_d^3} i b_1 \tag{1}$$

where k_d is the wavenumber in the medium around the array. ε_0 and ε_d are the vacuum dielectric constant and relative dielectric constant of the surrounding medium, respectively. a_1 and b_1 are the Mie coefficients of the ED and MD, respectively. Let us consider the interaction between dipoles under the normal incidence of electromagnetic waves. In this case, lattice sums G^0_{xx} and G^0_{yy} can be expressed through the contribution of the dipoles as

$$G^0_{xx,yy} = \sum_{n_x n_y} \frac{e^{ik_d D}}{4\pi D}\left[1 + \frac{i}{Dk_d} - \frac{1}{D^2k_d^2} - \frac{n^2_{x,y}}{D^2} - \frac{3in^2_{x,y}D^2_{x,y}}{D^2} + \frac{3n^2_{x,y}D^2_{x,y}}{D^4k_d^2}\right] \tag{2}$$

where $D = |d_l - d_j|$ and D are the distances between dipoles l and j. After considering the lattice sum, the effective polarizabilities can be expressed as

$$\alpha^E_{eff} = \frac{1}{\left(\frac{\varepsilon_0\varepsilon_d}{\alpha^E} - k_d^2 G^0_{xx}\right)},\ \alpha^M_{eff} = \frac{1}{\left(\frac{1}{\alpha^M} - k_d^2 G^0_{yy}\right)} \tag{3}$$

ED and MD appear when $Re[\varepsilon_0/\alpha^E - k_d^2 G^0_{xx}] = 0$ and $\mathrm{Re}[1/\alpha^M - k_d^2 G^0_{yy}] = 0$.

In this approach, the reflectance, transmittance, and absorptance can also be calculated from the effective polarizabilities.

$$R = \frac{k_d^2}{4S_L^2}([Re(\alpha^E_{eff}) - Re(\alpha^M_{eff})]^2 + [Im(\alpha^E_{eff}) - Im(\alpha^M_{eff})]^2) \tag{4}$$

$$T = \left[1 - \frac{k_d}{2S_L}[Im(\alpha^E_{eff}) + Im(\alpha^M_{eff})]\right]^2 + \frac{k_d^2}{4S_L^2}[Re(\alpha^E_{eff}) + Re(\alpha^M_{eff})]^2 \tag{5}$$

and

$$A = \frac{k_d}{S_L}[Im(\alpha^E_{eff}) + Im(\alpha^M_{eff})] - \frac{k_d^2}{2S_L^2}[Re(\alpha^E_{eff})^2 + Re(\alpha^M_{eff})^2 + Im(\alpha^E_{eff})^2 + Im(\alpha^M_{eff})^2] \tag{6}$$

where $S_L = D_x \times D_y$ is the array elementary cell; D_x and D_y are the dimensions of the cell in the x- and y-directions, respectively. The amplitude value of the reflectance coefficient can also be written as

$$r = (ik_d/2S_L)[\alpha^E_{eff} - \alpha^M_{eff}] \tag{7}$$

The reflectance is zero when the effective polarizabilities of the ED and MD are equal. This is because of the destructive interference between the electric and magnetic dipole responses of the nanoparticle array. This effect is called the lattice Kerker effect.[41] In the literature,[46] researchers used the Kerker effect with ED and MD coupling inside Ge nanodisks to demonstrate the superabsorbing devices by tuning the diameters of the nanoantennas. Using a different approach, we manipulated the EDLR to couple the MDR by tuning the transverse period (P_y) on the GNA and producing strong field

https://doi.org/10.1021/acsnano.1c11326
ACS Nano 2022, 16, 5994−6001

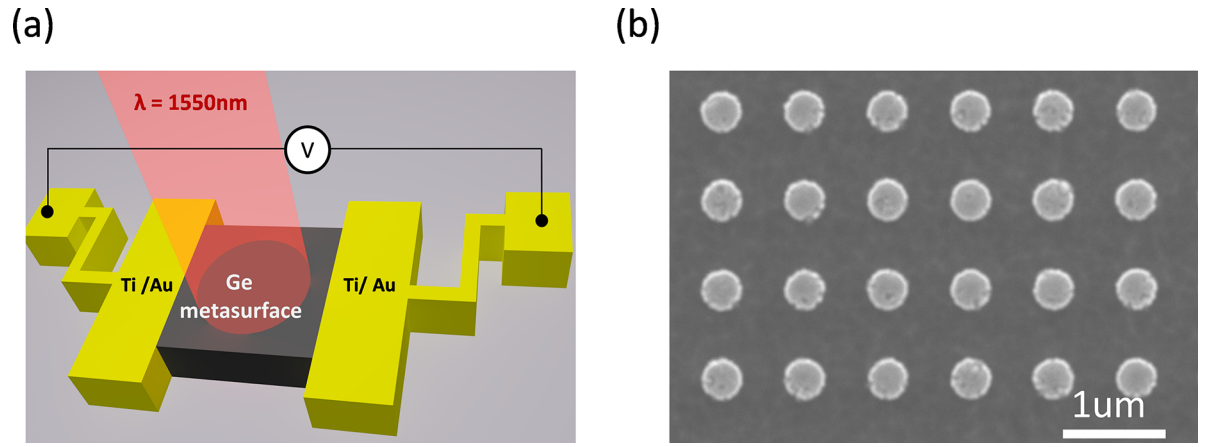

Figure 1. (a) Schematic of the Ge metasurface photodetector. A Ge metasurface is aligned to Au electrodes. (b) SEM image of the Ge metasurface from a top view.

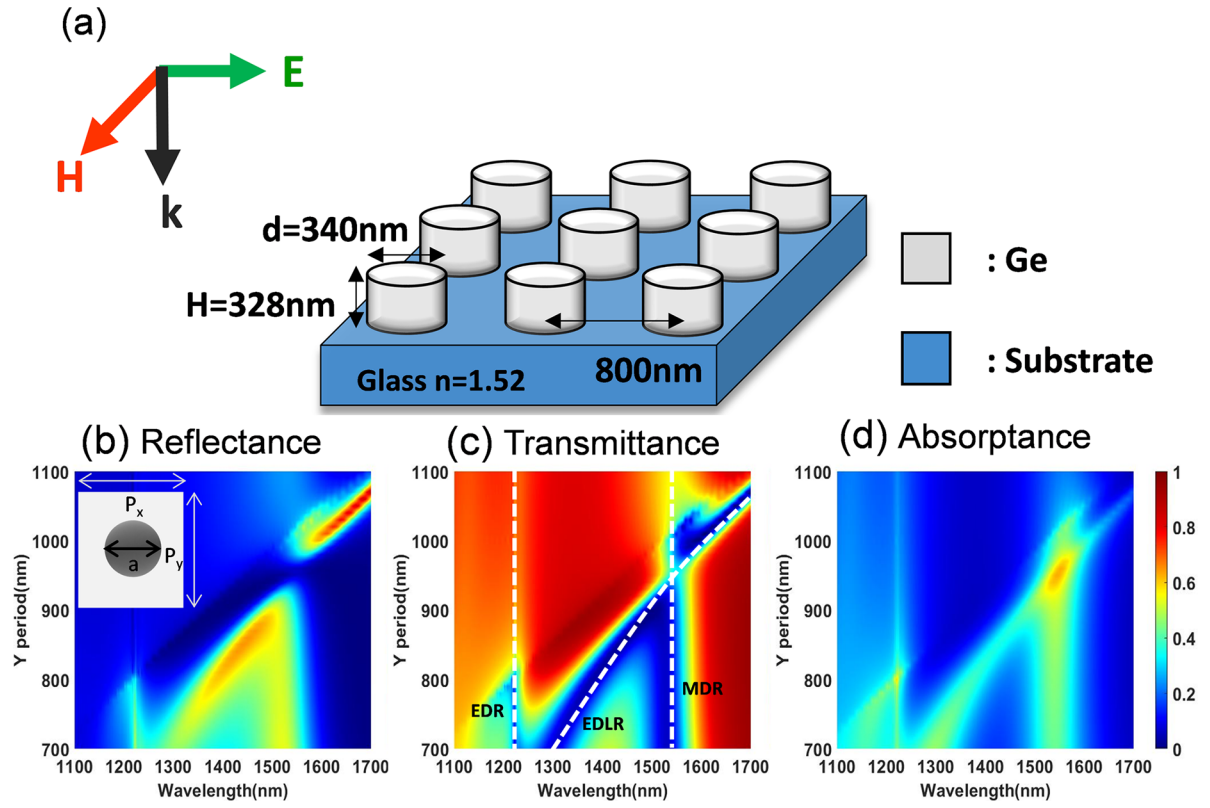

Figure 2. (a) Design of Ge metasurfaces, with d_1 = 340 nm, H_1 = 328 nm, and longitudinal period P_x = 800 nm on a glass substrate. We simulated a Ge absorber by tuning the transverse periods (P_y) of a GNA. (b) Reflectance, (c) transmittance, and (d) absorptance spectra with different P_y. The GNA is set on a glass substrate, and immersion oil is used as the surrounding medium (n = 1.516). The diameter of the GNA cylinder is 340 nm, the thickness is 328 nm, and P_x is 800 nm.

confinement to enhance the absorptance of the metasurfaces. Furthermore, we applied these effects to photocurrent detection and proposed a selective photodetector at the optical communication wavelength. Figure 1(a) shows a schematic of the device structure with a Ge metasurface surrounded on two sides with gold electrodes. Figure 1(b) shows the SEM images of the Ge metasurface from a top view.

RESULTS AND DISCUSSION

Design and Optical Characterization of the Absorber. To elucidate the optical response of the resonant nanoantenna array, we performed a numerical study using the finite-difference time-domain (FDTD) commercial software (Lumerical Inc.) and calculated the reflectance, transmittance, and absorptance spectra of the GNA arrays. We consider the periodic metasurface of Ge nanocylinder resonators with diameter a_1 = 340 nm and thickness h_1 = 328 nm. The GNA was fabricated on a glass substrate, and immersion oil was used as the upper surrounding medium (n = 1.516). Herein, for polarization along the x-axis and varied period P_y, the EDLR can be tuned to overlap with the magnetic dipole resonance (MDR) and produce destructive interference between them.

https://doi.org/10.1021/acsnano.1c11326
ACS Nano 2022, 16, 5994−6001

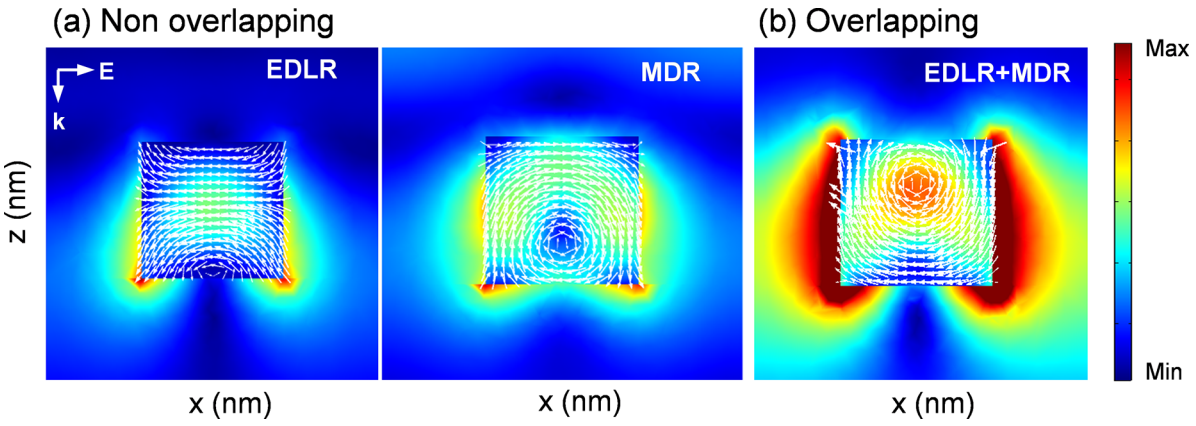

Figure 3. Electric field distributions of (a) nonoverlapping resonance with P_y = 800 nm (EDLR at ~1400 nm on the left-hand side and MDR at ~1550 nm on the right-hand side) and (b) overlapping resonances at ~1550 nm with P_y = 940 nm.

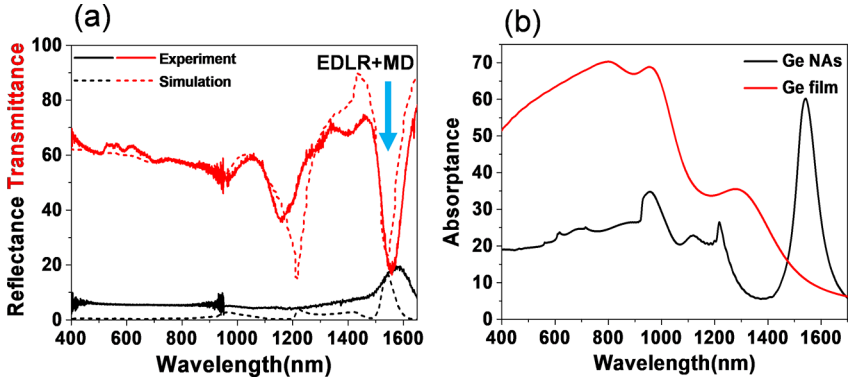

Figure 4. (a) Measured (solid line) results of reflectance (black line) and transmittance (red line) spectra with the transverse period P_y = 940 nm. (b) Comparison of the absorptance spectra of a GNA and Ge films with a thickness of 328 nm.

Figure 2 shows the schematics of the GNA absorbers as well as the reflectance, transmittance, and absorptance spectra of the metasurface. We fixed the longitudinal period, P_x, at 800 nm and excited the EDLR at a wavelength close to the Rayleigh anomaly, $\lambda_{EDLR} \approx \lambda_{RA} = nP_y$. The simulation results indicate that the Kerker condition is satisfied when the transverse period, P_y, is 940 nm, and the reflectance is suppressed. In nanoparticles with a small imaginary part of the refractive index (referred here as low-k), the energy of backward scattering can be transferred to forward scattering, which means that the transmittance is increased.[35,47] However, for nanoparticles with a large imaginary part of the refractive index (referred to here as high-k), the energy of forward scattering can be stored inside the particles, resulting in a low transmittance of light through the structure.[48−50] Ge has a moderate imaginary part of the refractive index at 1550 nm, which is sufficient to create the narrowband absorptance. The material loss affects the backward scattering transferred to forward scattering or stored inside (becoming absorptance), as proposed in our previous work.[42]

To illustrate and analyze the absorptance enhancement by confining strong optical near-fields in a subwavelength volume, as shown in Figure 3, we plot the electric field distribution. As shown in Figure 4(a), the x-polarized light is incident from the top to the GNA. First, the strong transmitted light intensities of EDLR and MDR are shown without overlapping. However, the reflectance and transmittance are reduced when EDLR and MDR overlap, and the absorptance is enhanced. These simulations confirm our hypothesis of favorable conditions, and Figure 3(b) shows that stronger electric field energy is confined in the GNA.

The transmission and reflection experimental results for the Ge metasurface over the wavelength ranging from 400 to 1700 nm are presented in Figure 4(a). The wavelength range was extended to the visible range to show the general tendency of the spectra. The measurement results (solid line) are consistent with the simulation results (dashed line). We achieved an overlap between EDLR and MDR at a wavelength of 1550 nm and generated approximately 60% of the light absorptance in the experiment. We compared the absorptance in the GNA and the absorptance in the Ge thin film of the same thickness at 1550 nm. As shown in Figure 4(b), the presence of the GNA increased the enhancement by 6-fold, as compared to the unpatterned Ge films. This proves that the GNA can detect light more efficiently and significantly improve the poor absorption of the device.

Photodetector and Photocurrent Measurements. For the photocurrent measurement, we consider a sample of a GNA fabricated on 300 nm SiO_2 and Si as a substrate. Thereafter, the GNA was used with parameters similar to those of the absorber design. As shown in Figure 5(a), the photodetector sample has d_2 = 360 nm, H_2 = 260 nm, and the remaining thickness 80 nm Ge film to transport the photoelectrons. As shown in Figure S7, the remaining thickness of Ge should be considered, and the Kerker effect is present. The simulated results indicate that the high absorption with the ideal remaining thickness of Ge is 80−90 nm at a wavelength of 1550 nm. Furthermore, we simulated

https://doi.org/10.1021/acsnano.1c11326
ACS Nano 2022, 16, 5994−6001

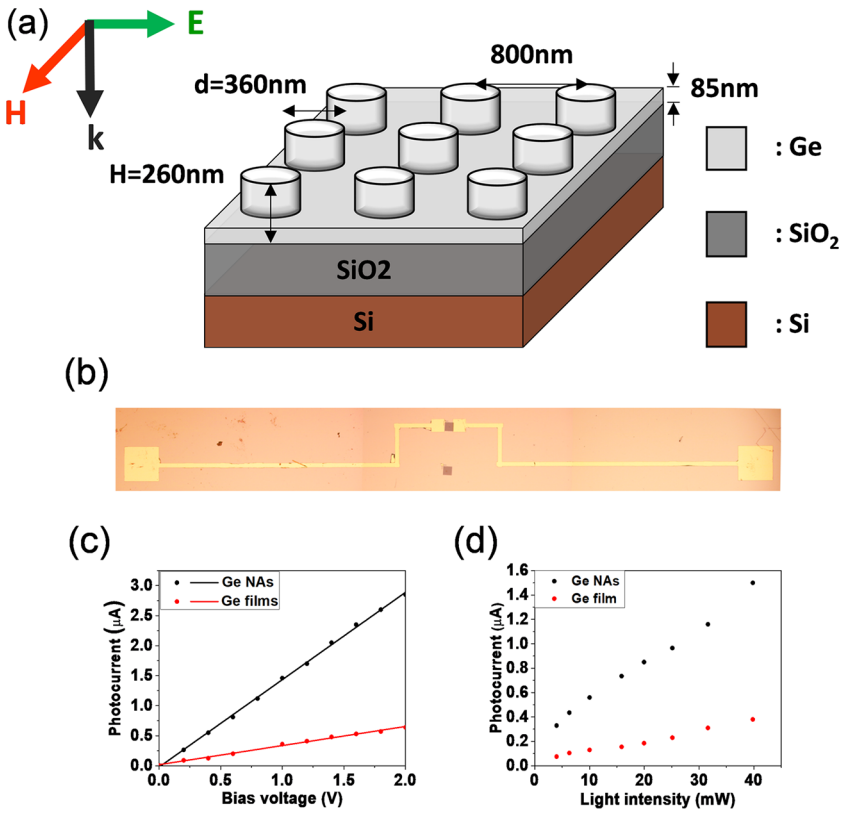

Figure 5. (a) Design of the Ge photodetector with d_2 = 360 nm, H_2 = 260 nm, P_x = 800 nm, and transverse period P_y = 830 nm on a 430 nm silicon dioxide layer and a Si substrate. (b) Microscope image of the GNA photodetector, top view. (c) Bias voltage dependence of GNA and Ge film photodetectors. The dots are experimental data, and the solid lines are linear fittings. (d) Photocurrent measured with a 1550 nm laser at a bias of 1 V with different light intensities.

a photodetector with different remaining thicknesses of Ge film. It shows that the absorptance is approximately 25% as the remaining thickness ranges from 50 to 70 nm. However, it has more absorptance enhancement with a remaining Ge film thickness of approximately 80−90 nm. By increasing the remaining thickness to over 95 nm, the absorptance would be below 50%. Evidently, a remaining thickness of 80 nm has a higher absorptance above 75%. Its bandwidth and quality factor are 13.88 nm and 110, respectively. Because hot-carrier generation depends on photon absorption, we integrated the electric field, which is proportional to the photocurrent response. We integrated the product of frequency ω, local electric field strength $|E|^2$, and the imaginary part of the dielectric permittivity over the full volume of the Ge metasurface, including the remaining Ge film, as mentioned by Bob et al.[51]

Figure 5(b) shows an optical microscope image of the Ge metasurface photodetector device. Light from the laser at a wavelength of 1550 nm was incident through a fiber on the metasurface. Figure 5(c) shows the voltage bias dependence of the photocurrent under 16 dBm laser illumination, and it compares with the Ge film and GNA devices. At a bias of +1 V, the photocurrent is enhanced by approximately 5 times at 1550 nm compared with the plane Ge film photodetector. Figure 5(d) shows the photocurrent versus light intensity under a bias of +1 V. As expected, the photocurrent increased almost linearly with 1550 nm light illumination from 4 to 40 mW.

As shown in Figure 6, we measured the responsivity of the photodetector when the laser was tuned from 1480 to 1580 nm, with a bias voltage of +1 V. The responsivity decreased

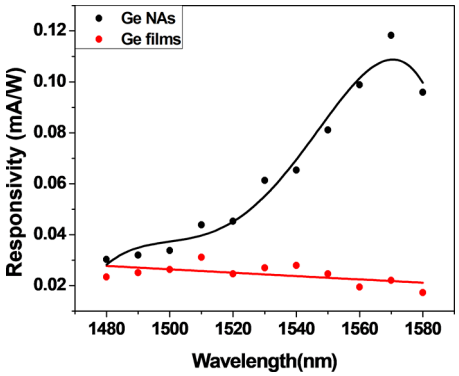

Figure 6. Measured responsivity of the Ge NAs and the plane Ge film at different wavelengths. The dots are experimental data; the black and red solid lines are fitting curves.

linearly for the plane Ge film. This simple dependence can be ascribed to the reduction in the absorption coefficient of Ge from 1480 to 1580 nm. The GNA photodetector has characteristic responsivity peaks at 1570 nm, which is very close to our designed resonant wavelength of 1550 nm. Overall, the characteristic responsivity of the GNA photodetector can be attributed to the enhanced absorption in the Ge metasurface resulting from the lattice Kerker effect. The deviation of the redshift in the simulation and responsivity of the photodetector was caused by the electrical measurement setup and roughness profile of the GNA in Figure S9.

https://doi.org/10.1021/acsnano.1c11326
ACS Nano 2022, 16, 5994−6001

CONCLUSIONS

In summary, we experimentally demonstrated a GNA metasurface photodetector with a strong absorption and high efficiency at telecommunication wavelengths. The strong localized electric fields inside the Ge nanoantennas are achieved because of the intrinsic loss of material and the overlap between the EDLR and MD resonances.

In optical spectral responsivity, compared with the Ge film with the same thickness, the GNA metasurface has a 6-fold absorptance enhancement. In addition, the photocurrent in the GNA metasurface photodetector increased by approximately 5 times compared with that of the pure Ge film photodetector. This is because of the interaction of the strong near-fields of the nanoparticles with semiconductors and further transformation of the optical energy into electricity. The experimentally demonstrated structures show a prominent responsivity feature at 1570 nm, which is very close to the designed resonant wavelength of 1550 nm. The device performance shows that a selective narrowband metasurface photodetector can be demonstrated using dielectric nanostructures in communication applications. When combined with the lattice Kerker effect, it can provide efficient applications for sensing, thermal emitters, optical filters, and imaging in the near future.

METHODS

Fabrication of the GNA Absorber. A 328 nm Ge film was deposited on a glass substrate through high-density plasma chemical vapor deposition (HDPCVD). The refractive index and thickness of the deposited films were characterized using a spectroscopic ellipsometry apparatus (SENTECH SENDIR). After deposition, a 250 nm photoresist PMMA A4 was coated on the top. Electron-beam lithography (ELIONIX, ELS-7500 EX) was used to define the nanoparticles in the structure. The 30 nm chromium films were deposited using an E-gun evaporator (ULVAC, VT1−10CE) as the etching mask. Thereafter, the lift-off process was used to define the etching area. Additionally, we used an ICP etcher (Model RIE-101iPH) with 10 sccm of CHF_3 plasma, an ICP power of 800 W, and an etching time of 65 s. This process produces a Ge metasurface with an active area of 100 × 100 μm. In the experiments, the active area of the metasurface was covered with immersion oil (n = 1.516) to match the refractive index of the superstrates and substrates.

Fabrication of the GNA Photodetector. Figure S3 shows the fabrication process of the GNA photodetector. The process began with a Si substrate and with the deposition of a 430 nm SiO_2 film via PECVD (Oxford, 100 PECVD cassette system). Additionally, a 260 nm Ge film was grown via HDPCVD. In addition to the optical constant and thickness of the Ge film, the E-beam lithography process and etching process were also characterized and fabricated using the same instrument as above. The GNA had a radius of 180 nm and a height of 260 nm. Here, an 80 nm thick Ge film remained at the bottom. To collect the photoelectrons effectively, gold electrodes were fabricated via electron-beam lithography to connect to both sides of the metasurface. During the experiments, the active area of the metasurface was covered by immersion oil (n = 1.516).

Optical Measurement Setup. As shown in Figure S1, the optical characteristics (reflectance and transmittance) of the absorber and photodetector samples were measured using a visible spectrum analyzer (Ocean optics UB2000), NIR spectrum analyzer (OtO photonics SW2540), and optical microscope (Olympus BX51). For the sample active area, we used an x-polarizer and pinhole, which can collect most of the normal incidence signal, through a 50× (N.A. = 0.5) objective lens. The absorber and photodetector were covered by immersion oil (n = 1.516) as the surrounding medium to match the refractive index of the superstrates and substrates.

ASSOCIATED CONTENT

Supporting Information

The Supporting Information is available free of charge at https://pubs.acs.org/doi/10.1021/acsnano.1c11326.

Figures: (S1) Schematic of the optical measurement; (S2) schematic diagram of the electrical measurement setup; (S3) the fabrication process of the GNA photodetector; (S4) simulations of germanium narrowband absorber photodetectors with the tuning of the transverse periods (P_y) of a GNA; (S5) electric field distributions of the GNA photodetector; (S6) the optical results in comparison to simulation and experimental measurements of the nanostructure; (S7) calculated absorptance of the different remaining thicknesses in Ge films and the integrated E-field in GNA photodetectors; (S8) absorptance measurement result and simulated analysis with numerical aperture (N.A. = 0.5); (S9) SEM image of the GNA photodetector; (S10) GNA responsivity and the calculated integrated E-field with a GNA radius of 210 nm; (S11) the laser moves and illuminates at different positions (1, 2, 3); (S12) the laser moves and illuminates at different positions (4, 5, 6) (PDF)

AUTHOR INFORMATION

Corresponding Author

Kuo-Ping Chen − *Institute of Imaging and Biomedical Photonics, National Yang Ming Chiao Tung University, Tainan 711, Taiwan;* orcid.org/0000-0001-6256-9145; Email: kpchen@nycu.edu.tw

Authors

Zhong-Xing Zhou − *Institute of Photonic System, National Yang Ming Chiao Tung University, Tainan 711, Taiwan*

Ming-Jyun Ye − *College of Photonics, National Yang Ming Chiao Tung University, Tainan 711, Taiwan;* orcid.org/0000-0003-2307-1461

Min-Wen Yu − *College of Photonics, National Yang Ming Chiao Tung University, Tainan 711, Taiwan;* orcid.org/0000-0003-4173-8813

Jhen-Hong Yang − *Institute of Photonic System, National Yang Ming Chiao Tung University, Tainan 711, Taiwan;* orcid.org/0000-0003-3176-5009

Kuan-Lin Su − *Institute of Lighting and Energy Photonics, National Yang Ming Chiao Tung University, Tainan 711, Taiwan*

Chung-Ching Yang − *Institute of Photonic System, National Yang Ming Chiao Tung University, Tainan 711, Taiwan*

Cheng-Yeh Lin − *Institute of Photonic System, National Yang Ming Chiao Tung University, Tainan 711, Taiwan*

Viktoriia E. Babicheva − *Department of Electrical and Computer Engineering, University of New Mexico, Albuquerque, New Mexico 87131, United States;* orcid.org/0000-0002-0789-5738

Ivan V. Timofeev − *Kirensky Institute of Physics, Federal Research Center KSC SB RAS, Krasnoyarsk 660036, Russia; Institute of Engineering Physics and Radioelectronics, Siberian Federal University, Krasnoyarsk 660041, Russia;* orcid.org/0000-0002-6558-5607

Complete contact information is available at: https://pubs.acs.org/10.1021/acsnano.1c11326

https://doi.org/10.1021/acsnano.1c11326
ACS Nano 2022, 16, 5994−6001

Author Contributions

[#]Z.-X.Z. and M.-J.Y. contributed equally.

Author Contributions

Z.-X.Z. performed the sample fabrication, simulation, and optical characterization. M.-J.Y. and M.-W.Y. improved the work during the rebuttal. V.E.B. and Z.-X.Z. conducted the theoretical model. M.-J.Y., M.-W.Y., J.-H.Y., K.-L.S., C.-C.Y., I.V.T., and C.-Y.L. helped to analyze the experimental data. Z.-X.Z., M.-J.Y., V.E.B., and K.-P.C. wrote and revised the manuscript. All authors discussed the results and commented on the manuscript.

Notes

The authors declare no competing financial interest.

ACKNOWLEDGMENTS

We are grateful to Prof. Chun-Ting Lin and Prof. Chien-Chung Lin for helpful discussions. This work was supported by the Higher Education Sprout Project of the National Yang Ming Chiao Tung University and Ministry of Education and the Ministry of Science and Technology (MOST-111-2923-E-A49-001-MY3; 108-2923-E-009-003-MY3; 110-2224-E-009-002; 109-2628-E-009-007-MY3; 110-2221-E-A49-019-MY3). This research was also funded by the Russian Science Foundation (project no. 22-42-08003).

REFERENCES

(1) Jalali, B.; Fathpour, S. Silicon Photonics. *J. Lightwave Technol.* **2006**, *24* (12), 4600−4615.
(2) Thomson, D.; Zilkie, A.; Bowers, J. E.; Komljenovic, T.; Reed, G. T.; Vivien, L.; Marris-Morini, D.; Cassan, E.; Virot, L.; Fédéli, J.-M.; et al. Roadmap on silicon photonics. *Journal of Optics* **2016**, *18* (7), 073003.
(3) Won, R. Integrating silicon photonics. *Nat. Photonics* **2010**, *4* (8), 498−499.
(4) Almeida, V. R.; Barrios, C. A.; Panepucci, R. R.; Lipson, M. All-optical control of light on a silicon chip. *Nature* **2004**, *431* (7012), 1081−1084.
(5) Doylend, J. K.; Knights, A. P. The evolution of silicon photonics as an enabling technology for optical interconnection. *Laser & Photonics Reviews* **2012**, *6* (4), 504−525.
(6) Liu, J.-M. Semiconductor optoelectronics. In *Photonic devices*; Cambridge University Press: Cambridge, 2005; pp 757−1017.
(7) Liu, C.; Guo, J.; Yu, L.; Li, J.; Zhang, M.; Li, H.; Shi, Y.; Dai, D. Silicon/2D-material photodetectors: from near-infrared to mid-infrared. *Light: Science & Applications* **2021**, *10* (1), 123.
(8) Akinwande, D.; Huyghebaert, C.; Wang, C.-H.; Serna, M. I.; Goossens, S.; Li, L.-J.; Wong, H.-S. P.; Koppens, F. H. Graphene and two-dimensional materials for silicon technology. *Nature* **2019**, *573* (7775), 507−518.
(9) Asghari, M.; Krishnamoorthy, A. V. Energy-efficient communication. *Nat. Photonics* **2011**, *5* (5), 268−270.
(10) Michel, J.; Liu, J.; Kimerling, L. C. High-performance Ge-on-Si photodetectors. *Nat. Photonics* **2010**, *4* (8), 527−534.
(11) Kang, Y.; Liu, H.-D.; Morse, M.; Paniccia, M. J.; Zadka, M.; Litski, S.; Sarid, G.; Pauchard, A.; Kuo, Y.-H.; Chen, H.-W.; et al. Monolithic germanium/silicon avalanche photodiodes with 340 GHz gain-bandwidth product. *Nat. Photonics* **2009**, *3* (1), 59−63.
(12) Cao, L.; Park, J. S.; Fan, P.; Clemens, B.; Brongersma, M. L. Resonant germanium nanoantenna photodetectors. *Nano Lett.* **2010**, *10* (4), 1229−33.
(13) Lischke, S.; Peczek, A.; Morgan, J.; Sun, K.; Steckler, D.; Yamamoto, Y.; Korndörfer, F.; Mai, C.; Marschmeyer, S.; Fraschke, M.; et al. Ultra-fast germanium photodiode with 3-dB bandwidth of 265 GHz. *Nat. Photonics* **2021**, 1−7.
(14) Morse, M.; Dosunmu, O.; Sarid, G.; Chetrit, Y. Performance of Ge-on-Si pin photodetectors for standard receiver modules. *IEEE Photonics Technology Letters* **2006**, *18* (23), 2442−2444.
(15) Shi, S.; Pacifici, D.; Zaslavsky, A. Fast and efficient germanium quantum dot photodetector with an ultrathin active layer. *Appl. Phys. Lett.* **2021**, *119* (22), 221108.
(16) DeRose, C. T.; Trotter, D. C.; Zortman, W. A.; Starbuck, A. L.; Fisher, M.; Watts, M. R.; Davids, P. S. Ultra compact 45 GHz CMOS compatible Germanium waveguide photodiode with low dark current. *Opt. Express* **2011**, *19* (25), 24897−24904.
(17) Virot, L.; Crozat, P.; Fédéli, J.-M.; Hartmann, J.-M.; Marris-Morini, D.; Cassan, E.; Boeuf, F.; Vivien, L. Germanium avalanche receiver for low power interconnects. *Nat. Commun.* **2014**, *5* (1), 4957.
(18) Benedikovic, D.; Cassan, E.; Marris-Morini, D.; Baudot, C.; Boeuf, F.; Fedeli, J.-M.; Kopp, C.; Vivien, L.; Virot, L.; Aubin, G.; et al. Comprehensive study on chip-integrated germanium pin photodetectors for energy-efficient silicon interconnects. *IEEE J. Quantum Electron.* **2020**, *56* (1), 1−9.
(19) Boukari, H.; Lagakos, N. Determination of the optical constants by Brillouin scattering. *Handbook of optical constants of solids* **1997**, *3*, 121−154.
(20) Xia, Z.; Song, H.; Kim, M.; Zhou, M.; Chang, T.-H.; Liu, D.; Yin, X.; Xiong, K.; Mi, H.; Wang, X.; et al. Single-crystalline germanium nanomembrane photodetectors on foreign nanocavities. *Science advances* **2017**, *3* (7), No. e1602783.
(21) Yang, F.; Cong, H.; Yu, K.; Zhou, L.; Wang, N.; Liu, Z.; Li, C.; Wang, Q.; Cheng, B. Ultrathin broadband germanium-graphene hybrid photodetector with high performance. *ACS Appl. Mater. Interfaces* **2017**, *9* (15), 13422−13429.
(22) Kim, M.; Liu, S.-C.; Kim, T. J.; Lee, J.; Seo, J.-H.; Zhou, W.; Ma, Z. Light absorption enhancement in Ge nanomembrane and its optoelectronic application. *Opt. Express* **2016**, *24* (15), 16894−16903.
(23) Kim, M.; Seo, J.-H.; Yu, Z.; Zhou, W.; Ma, Z. Flexible germanium nanomembrane metal-semiconductor-metal photodiodes. *Appl. Phys. Lett.* **2016**, *109* (5), 051105.
(24) Cho, M.; Seo, J.-H.; Kim, M.; Lee, J.; Liu, D.; Zhou, W.; Yu, Z.; Ma, Z. Resonant cavity germanium photodetector via stacked single-crystalline nanomembranes. *Journal of Vacuum Science & Technology B, Nanotechnology and Microelectronics: Materials, Processing, Measurement, and Phenomena* **2016**, *34* (4), 040604.
(25) Song, J.; Yuan, S.; Cui, C.; Wang, Y.; Li, Z.; Wang, A. X.; Zeng, C.; Xia, J. High-efficiency and high-speed germanium photodetector enabled by multiresonant photonic crystal. *Nanophotonics* **2021**, *10* (3), 1081−1087.
(26) Son, B.; Lin, Y.; Lee, K. H.; Wang, Y.; Wu, S.; Tan, C. S. High speed and ultra-low dark current Ge vertical pin photodetectors on an oxygen-annealed Ge-on-insulator platform with GeO x surface passivation. *Opt. Express* **2020**, *28* (16), 23978−23990.
(27) Wall, B.; Amsbaugh, J. F.; Beglarian, A.; Bergmann, T.; Bichsel, H.; Bodine, L.; Boyd, N.; Burritt, T. H.; Chaoui, Z.; Corona, T.; et al. Dead layer on silicon p-i-n diode charged-particle detectors. *Nuclear Instruments and Methods in Physics Research Section A: Accelerators, Spectrometers, Detectors and Associated Equipment* **2014**, *744*, 73−79.
(28) Gomez-Medina, R.; Garcia-Camara, B.; Suárez-Lacalle, I.; González, F.; Moreno, F.; Nieto-Vesperinas, M.; Sáenz, J. J. Electric and magnetic dipolar response of germanium nanospheres: interference effects, scattering anisotropy, and optical forces. *Journal of Nanophotonics* **2011**, *5* (1), 053512.
(29) Ishii, S.; Chen, K.; Okuyama, H.; Nagao, T. Resonant optical absorption and photothermal process in high refractive index germanium nanoparticles. *Advanced Optical Materials* **2017**, *5* (5), 1600902.
(30) Kuznetsov, A. I.; Miroshnichenko, A. E.; Brongersma, M. L.; Kivshar, Y. S.; Luk'yanchuk, B. Optically resonant dielectric nanostructures. *Science* **2016**, *354* (6314), aag2472.
(31) García-Cámara, B.; Moreno, F.; González, F.; Martin, O. J. Light scattering by an array of electric and magnetic nanoparticles. *Opt. Express* **2010**, *18* (10), 10001−10015.

https://doi.org/10.1021/acsnano.1c11326
ACS Nano 2022, 16, 5994−6001

(32) García-Cámara, B.; de La Osa, R. A.; Saiz, J.; González, F.; Moreno, F. Directionality in scattering by nanoparticles: Kerker's null-scattering conditions revisited. *Optics letters* **2011**, *36* (5), 728−730.
(33) Alù, A.; Engheta, N. How does zero forward-scattering in magnetodielectric nanoparticles comply with the optical theorem? *Journal of Nanophotonics* **2010**, *4* (1), 041590.
(34) Luk'yanchuk, B. S.; Voshchinnikov, N. V.; Paniagua-Domínguez, R.; Kuznetsov, A. I. Optimum forward light scattering by spherical and spheroidal dielectric nanoparticles with high refractive index. *ACS Photonics* **2015**, *2* (7), 993−999.
(35) Shibanuma, T.; Albella, P.; Maier, S. A. Unidirectional light scattering with high efficiency at optical frequencies based on low-loss dielectric nanoantennas. *Nanoscale* **2016**, *8* (29), 14184−14192.
(36) Kerker, M.; Wang, D.-S.; Giles, C. Electromagnetic scattering by magnetic spheres. *JOSA* **1983**, *73* (6), 765−767.
(37) Baur, S.; Sanders, S.; Manjavacas, A. Hybridization of lattice resonances. *ACS Nano* **2018**, *12* (2), 1618−1629.
(38) Swiecicki, S. D.; Sipe, J. Surface-lattice resonances in two-dimensional arrays of spheres: multipolar interactions and a mode analysis. *Phys. Rev. B* **2017**, *95* (19), 195406.
(39) Zakomirnyi, V.; Ershov, A.; Gerasimov, V.; Karpov, S.; Ågren, H.; Rasskazov, I. Collective lattice resonances in arrays of dielectric nanoparticles: a matter of size. *Optics letters* **2019**, *44* (23), 5743−5746.
(40) Wang, W.; Ramezani, M.; Väkeväinen, A. I.; Törmä, P.; Rivas, J. G.; Odom, T. W. The rich photonic world of plasmonic nanoparticle arrays. *Mater. Today* **2018**, *21* (3), 303−314.
(41) Babicheva, V. E.; Evlyukhin, A. B. Resonant lattice Kerker effect in metasurfaces with electric and magnetic optical responses. *Laser & Photonics Reviews* **2017**, *11* (6), 1700132.
(42) Yang, C.-Y.; Yang, J.-H.; Yang, Z.-Y.; Zhou, Z.-X.; Sun, M.-G.; Babicheva, V. E.; Chen, K.-P. Nonradiating silicon nanoantenna metasurfaces as narrowband absorbers. *Acs Photonics* **2018**, *5* (7), 2596−2601.
(43) Evlyukhin, A. B.; Reinhardt, C.; Seidel, A.; Luk'yanchuk, B. S.; Chichkov, B. N. Optical response features of Si-nanoparticle arrays. *Phys. Rev. B* **2010**, *82* (4), 045404.
(44) Babicheva, V. E.; Evlyukhin, A. B. Interplay and coupling of electric and magnetic multipole resonances in plasmonic nanoparticle lattices. *MRS Commun.* **2018**, *8* (3), 712−717.
(45) Evlyukhin, A. B.; Reinhardt, C.; Zywietz, U.; Chichkov, B. N. Collective resonances in metal nanoparticle arrays with dipole-quadrupole interactions. *Phys. Rev. B* **2012**, *85* (24), 245411.
(46) Tian, J.; Luo, H.; Li, Q.; Pei, X.; Du, K.; Qiu, M. Near-Infrared Super-Absorbing All-Dielectric Metasurface Based on Single-Layer Germanium Nanostructures. *Laser & Photonics Reviews* **2018**, *12* (9), 1800076.
(47) Staude, I.; Miroshnichenko, A. E.; Decker, M.; Fofang, N. T.; Liu, S.; Gonzales, E.; Dominguez, J.; Luk, T. S.; Neshev, D. N.; Brener, I.; et al. Tailoring directional scattering through magnetic and electric resonances in subwavelength silicon nanodisks. *ACS Nano* **2013**, *7* (9), 7824−7832.
(48) Weng, Z.; Guo, Y. Broadband perfect optical absorption by coupled semiconductor resonator-based all-dielectric metasurface. *Materials* **2019**, *12* (8), 1221.
(49) Liu, X.; Fan, K.; Shadrivov, I. V.; Padilla, W. J. Experimental realization of a terahertz all-dielectric metasurface absorber. *Opt. Express* **2017**, *25* (1), 191−201.
(50) Babicheva, V. E. Lattice Kerker effect in the array of hexagonal boron nitride antennas. *MRS Advances* **2018**, *3* (45−46), 2783−2788.
(51) Zheng, B. Y.; Zhao, H.; Manjavacas, A.; McClain, M.; Nordlander, P.; Halas, N. J. Distinguishing between plasmon-induced and photoexcited carriers in a device geometry. *Nat. Commun.* **2015**, *6*, 7797.

https://doi.org/10.1021/acsnano.1c11326
ACS Nano 2022, 16, 5994−6001